Supporting Information

Rapid and Energy-Efficient Microwave Pyrolysis for High-Yield Production of Highly-Active Bifunctional Electrocatalysts for Water Splitting

Huawei Huang, Si Zhou, Chang Yu, Hongling Huang, Jijun Zhao, Liming Dai,* and Jieshan Qiu**

Experimental Section

Chemicals. Cobalt nitrate hexahydrate (Tianjin Kemiou, ⩾98.5%), zinc nitrate hexahydrate (Tianjin Kemiou, ⩾98.0%), 2-methylimidazole (Tianjin Guangfu, ⩾98.0%), 1,4-benzenedicarboxylic acid (Aladdin, 99.0%), nickel nitrate hexahydrate (Tianjin Kemiou, ⩾98%), iron chloride hexahydrate (Sinopharm Chemical Reagent Co., Ltd ⩾99.0 %), RuO_2 (Aladdin, Product No. R111923, 99.9%) and Pt/C (Shanghai Hesen, Product No. HPT020, Pt 20wt%) were used without any further purification. Commercial CF (TGP-H090) was purchased from Toray Industries.

Synthesis of Co-MOF/CF. Firstly, the commercial CF was functionalized by acid.[1] Then, 0.657 g 2-methylimidazole and 0.291 g cobalt nitrate hexahydrate were dissolved in 20 mL deionized water, respectively. Subsequently, the two solutions were mixed in a 50 mL beaker, and a piece of pre-treated CF was quickly vertically placed in the mixed solution. After reaction for five hours at 25 ^{o}C, the sample was rinsed and dried to obtain the Co-MOF/CF precursor.

Synthesis of Co-NC/CF. A piece of the obtained Co-MOF/CF precursor was put in a quartz reactor surrounded by graphene powder and underwent microwave irradiation in a modified household microwave oven (2.45 GHz, 800 W) for 60 s in Ar atmosphere, producing Co-NC/CF (mass loading: 1.1 mg cm^{-2}). The graphene powder can be recycled (Figure S1). The mass loading of active Co-NC in the as-prepared Co-NC/CF was obtained by a precision electronic balance (Mettler-Toledo XS205).

Synthesis of Co-NC-T/CF and CoO-NC-T/CF. A piece of the obtained Co-MOF/CF was also annealed at 800 ^{o}C for 1 h (heating rate: 5 ^{o}C min^{-1}) in Ar/H_2 (*ca.* 10 vol.% H_2) and Ar atmosphere in an electric tube furnace (power: 1000 W), respectively, yielding Co-NC-T/CF and CoO-NC-T/CF.

Synthesis of NC/CF. The NC/CF was synthesized with the same procedures described above for Co-NC/CF, except the 0.291 g cobalt nitrate hexahydrate were replaced with 0.297 g zinc nitrate hexahydrate in the synthesis of MOF precursor.

Synthesis of Ni-MOF, Ni-MOF-M, and Ni-MOF-T. Ni-MOF was synthesized by hydrothermal method.[2] Firstly, solution A was prepared by dissolving 5 mmol of 1,4-benzenedicarboxylic acid in 15 mL of N,N-dimethylmethanamide, and solution B was prepared by dissolving 5 mmol of nickel nitrate hexahydrate in 15 mL of water. Then the solution A and solution B were mixed and transferred into a 50 mL Teflon liner hydrothermal reactor and heated to 180 ^{o}C for 24 h. After the reaction is completed, Ni-MOF can be obtained. Ni-MOF-M was prepared by microwave treatment of Ni-MOF tablet surrounded by graphene powder for 60 s in Ar atmosphere. Ni-MOF-T was synthesized by annealing of Ni-MOF at 800 °C for 1 h (heating rate: 5 °C min^{-1}) under Ar atmosphere in an electric tube furnace.

Synthesis of Fe-MOF, Fe-MOF-M, and Fe-MOF-T. The Fe-MOF were synthesized according to the previously reported hydrothermal method.[3] Briefly, 0.16 g of F127 was dissolved in 15 ml of water, and 0.179 g of iron chloride hexahydrate was added into the solution. The resulting solution is stirred for 1 h before 0.6 ml of acetic acid is injected. After the mixture was stirred for another hour, 0.06 g of 2-aminoterephthalic acid is added. The reaction mixture was stirred for another 2 h. Afterwards, the mixture was transferred into an autoclave and crystallized for 24 h at 110 °C. After the reaction is completed, Fe-MOF can be obtained. Fe-MOF-M and Fe-MOF-T were synthesized by following the same procedure for the preparation of Ni-MOF-M and Ni-MOF-T.

Synthesis of NiCo-MOF, NiCo-MOF-M, and NiCo-MOF-T. For the preparation of NiCo-MOF,[4] 215 mg of nickel nitrate hexahydrate, 215 mg of cobalt nitrate hexahydrate, 150 mg of trimesic acid, and 1 g of polyvinylpyrrolidone were dissolved in 30 mL N,N-dimethylmethanamide solution. The obtained mixture was magnetically stirred for 10 min to ensure complete dissolution of the reactants, and was then transferred into Teflon-lined hydrothermal reactor and maintained at 150 °C for 6 h in an oven. After the reaction is completed, NiCo-MOF can be obtained. NiCo-MOF-M and NiCo-MOF-T were synthesized by following the same procedure for the preparation of Ni-MOF-M and Ni-MOF-T.

Materials Characterization. The as-made samples were characterized by SEM (FEI NOVA NanoSEM 450, HITACHI UHR FE-SEM SU8220), thermogravimetric analysis apparatus (STA 449 F3), XRD (SmartLab, 9KW, Cu Kα, λ=1.5406 Å), XPS (Thermo ESCALAB 250), TEM (TEM, Tecnai F30) and DXR Raman microscope (Thermo Fisher).

Electrochemical Characterization. Electrochemical measurements were carried out in 1 M KOH, in which a carbon rod was used as counter electrode and a saturated Ag/AgCl as the reference electrode in a three-electrode system controlled by a CHI 760E electrochemistry workstation. The polarization curves were measured at a scan rate of 5 mV s^{-1}. All the potentials reported in our work were versus RHE. EIS was performed at a potential of 1.55 V vs. RHE from 100 000 to 0.1 Hz by applying an amplitude of 5 mV in 1 M KOH. For evaluating the ECSA, the C_{dl} of electrocatalysts was measured by using cyclic voltammograms in a no Faradaic reaction potential window (1.20 - 1.30 V vs. RHE) at the scan rates of 5, 10, 15, 20, and 25 mV s^{-1}, respectively. The plot of the current density differences ($\Delta J = (J_a - J_c)$ at 1.25 V vs. RHE) against the different scan rates has a linear relationship and its slope is twice of the C_{dl}. In 1 M KOH, E (RHE) = E (Ag/AgCl) + 0.197 V + 0.059 V × pH.

Computational methods. Spin-polarized density functional theory (DFT) calculations were carried out by the Vienna ab initio simulation package (VASP),[5] using the planewave basis with an energy cutoff of 500 eV, the projector augmented wave pseudopotentials,[6] and the generalized gradient approximation parameterized by Perdew, Burke and Ernzerhof (GGA-PBE) for exchange-correlation functional.[7] The Co, CoO, RuO_2 and Pt solids were modeled by four-layer slabs with their (111), (100), (110) and (111) surfaces exposed, and the supercells consists of 2 × 1, 2 × 1, 2 × 2, and

2 × 2 unit cells for the lateral dimensions, respectively. For the Co-NC heterostructure, we used a supercell including 4 × 4 unit cells for graphene and Co(111) surface (modeled by four-layer slab). The in-plane lattice of Co is slightly compressed to fit that of graphene, giving lattice mismatch of 1.99%. Then, one N atom was substituted into the graphene sheet, resulting in doping concentration of 3.12 at.%, close to the experimental value (4.5 at.%). For all the models, a vacuum space of 16 Å thickness was applied to the vertical direction. The Brillouin zones of the supercells were sampled by uniform k point mesh with density larger than 0.03 $Å^{-1}$. With fixed cell parameters, the model structures were fully optimized using the convergence criteria of 10^{-4} eV for the electronic energy and 10^{-2} eV/Å for the forces on each atom. The bottom layer of metal (oxygen) atoms were fixed during structure relaxation to mimic semi-infinite solids. Grimme's semiempirical DFT-D3 scheme of dispersion correction was adopted to describe the van der Waals (vdW) interactions in layered materials.[8]

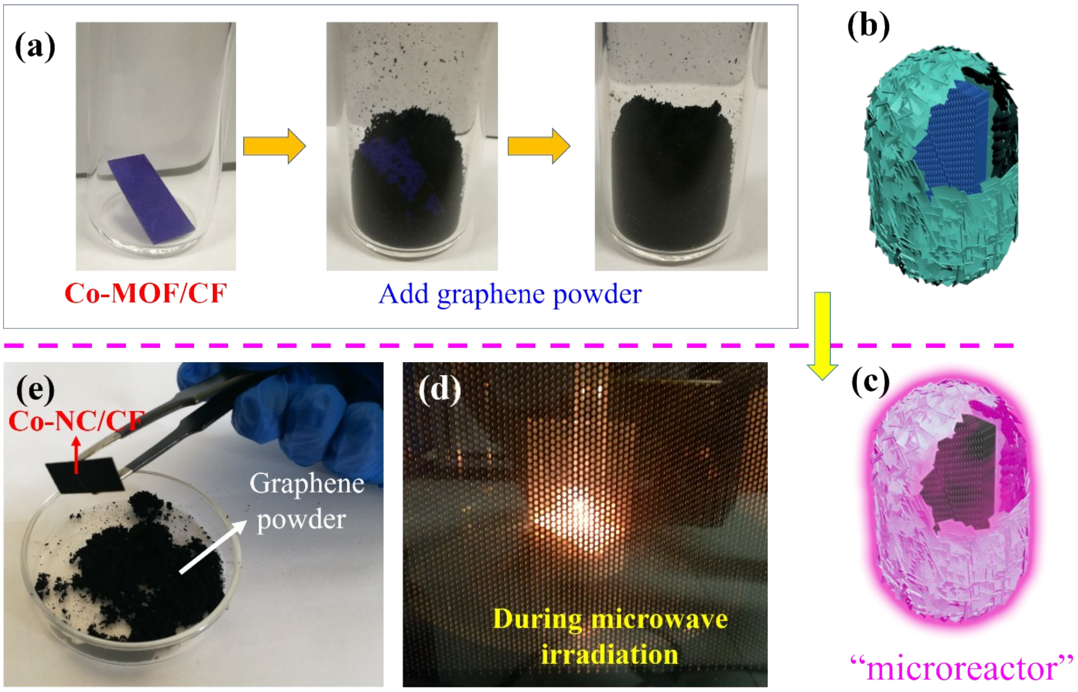

Figure S1. The detailed preparation processes of Co-NC/CF from Co-MOF/CF precursor: (a) the digital photographs of preparation process for Co-MOF/CF surrounded by graphene powder; (b) schematic diagram of Co-MOF/CF surrounded by graphene powder; (c) schematic diagram and (d) digital photograph of Co-MOF/CF surrounded by graphene powder during microwave irradiation; (e) the separation of as-made Co-NC/CF and graphene powder.

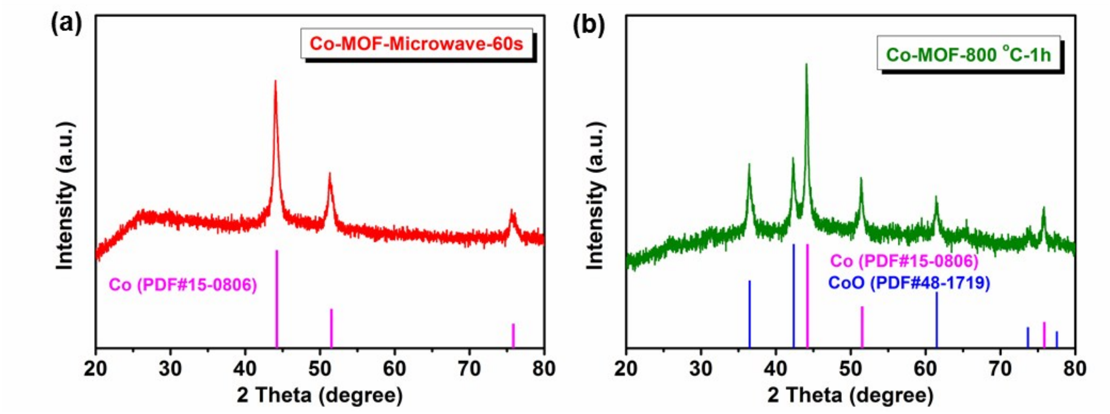

Figure S2. XRD patterns of (a) Co-MOF-Microwave-60s and (b) Co-MOF-800 ^{o}C-1h.

Notes: Compared to self-standing CoO-NC-T/CF (only CoO phase, Figure 3a in main text) prepared by the same procedure, the powder Co-MOF-800 ^{o}C-1h in the absence of CF shows metallic Co and CoO two species peaks, which is mainly because the Co-MOF powder is stacked together, thus may preventing diffusion and limiting the escape of small molecules during the heat treatment to some extent and further facilitating the reduction of partial Co species to metallic Co. While the open structure of the self-supporting materials causes the rapid escape of small molecules for Co-MOF/CF precursor during the slow heating process.

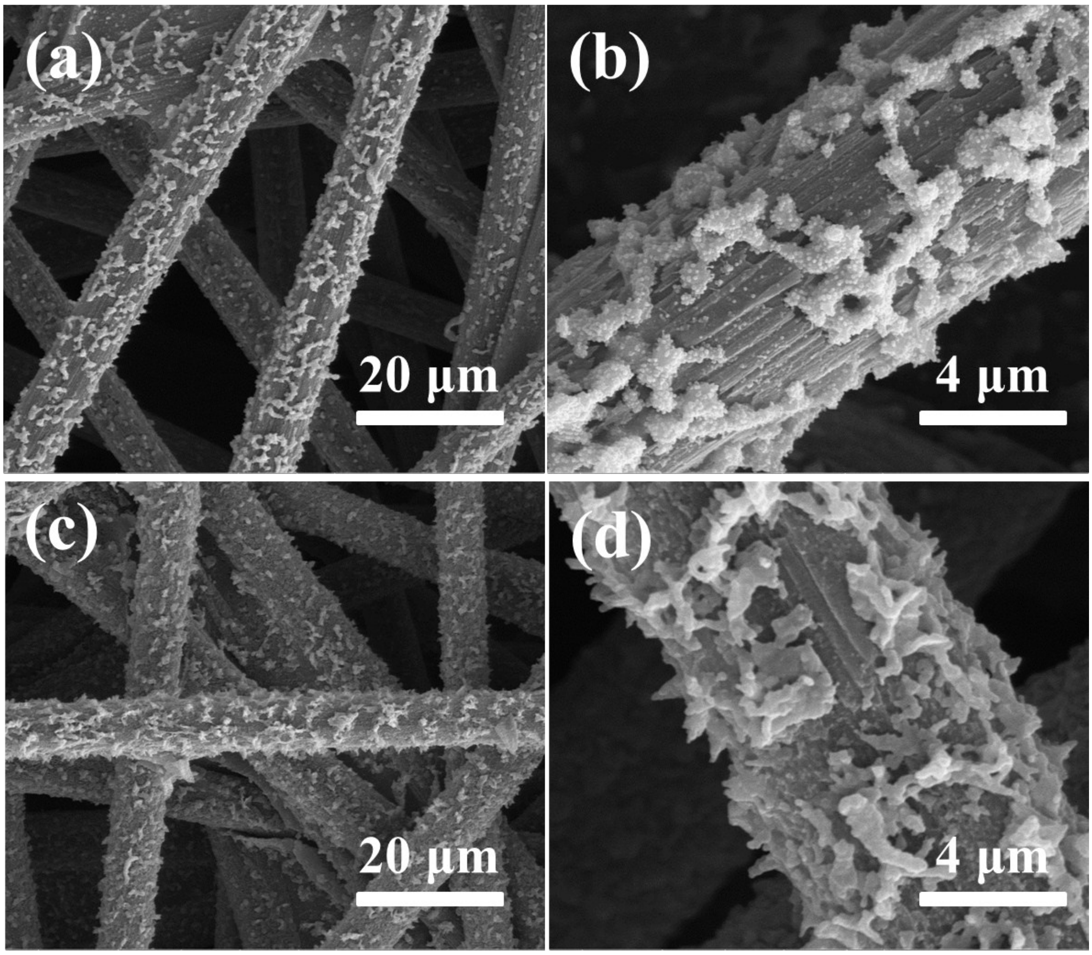

Figure S3. SEM images of (a, b) Co-NC-T/CF (pyrolyzed in Ar/H_2 atmosphere) and (c, d) CoO-NC-T/CF (pyrolyzed in Ar atmosphere).

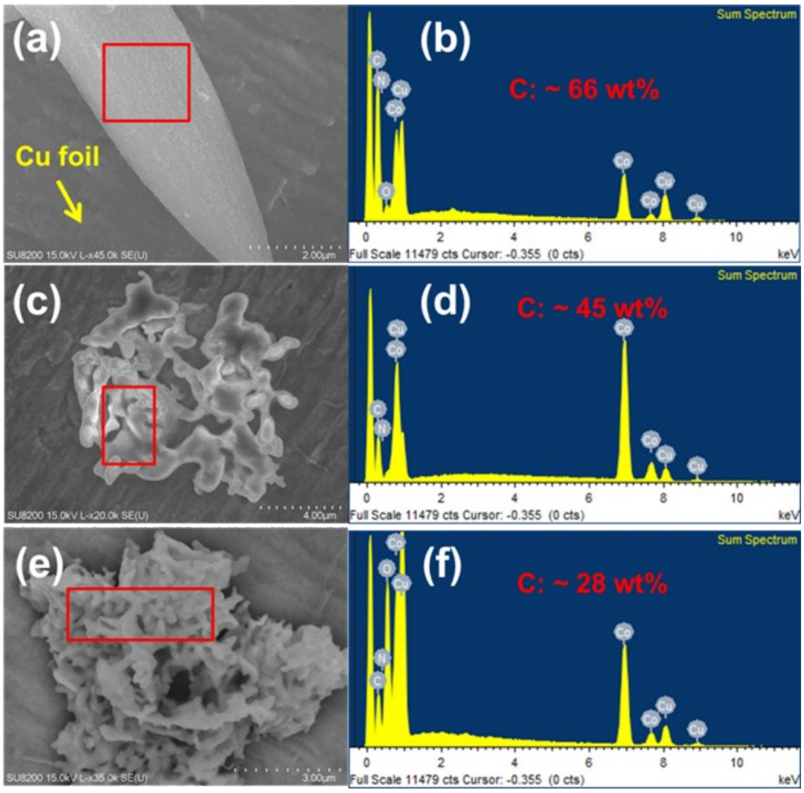

Figure S4. SEM images and their corresponding energy-dispersive X-ray (EDX) spectra of (a, b) Co-NC/CF, (c, d) Co-NC-T/CF, and (e, f) CoO-NC-T/CF. The red wire frame is the selected area for EDX detection.

Test method: Take a piece of the as-prepared self-standing catalyst and put it into ethanol. Then, the mixture was treated by strong ultrasonication treatment, in which the nanosheets/particles detached from CF substrate and formed the suspension. The catalyst-containing suspension was dropped on the copper foil and dried for SEM and EDX characterization.

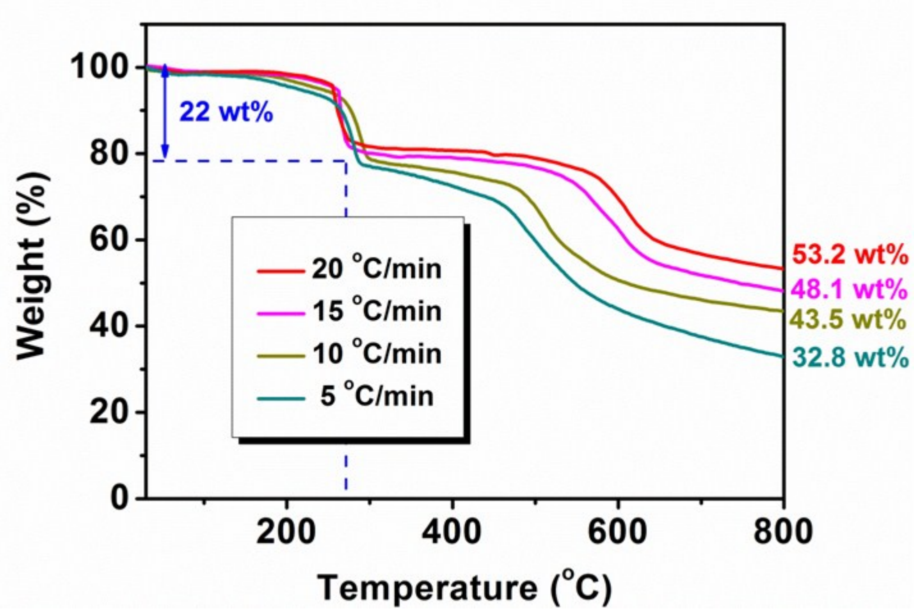

Figure S5. Thermogravimetric analysis (TGA) curves of Co-MOF powder tested at ramp rates of 5, 10, 15 and 20 °C min^{-1} under N_2 flow.

The first weight-loss step was measured to be *ca.* 22 wt% when the temperature was increased from 30 °C to 280 °C, corresponding to the elimination of bound water molecules.[9] The second weight-loss step was ascribed to the decomposition of organic ligands. It can be clearly noted that as the heating rate increased, the weight loss decreased and mass of the corresponding final product increased. This indicates more organic ligands in the Co-MOF were able to be converted into carbon. Traditional pyrolysis process was carried out at an elevated temperature and achieved in several hours, which led to low product yield derived from the above results. For microwave pyrolysis process, the system can reach more than 1000 °C in 10 s, implying a remarkable carbon fixation capacity.

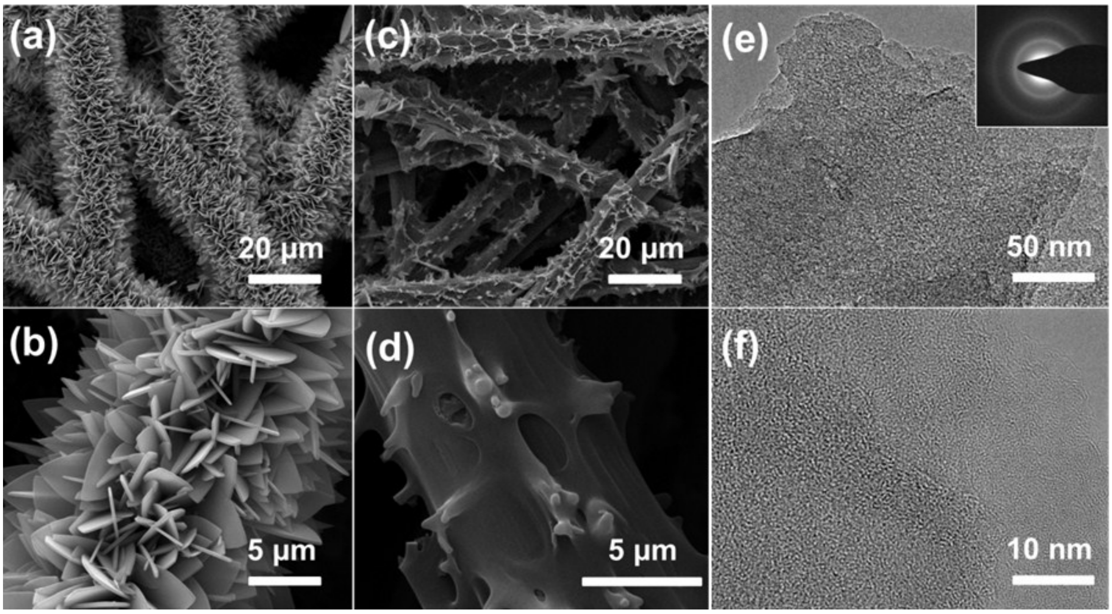

Figure S6. SEM images of (a, b) Zn-MOF/CF and (c, d) NC/CF; (e, f) TEM and HR-TEM images of NC/CF.

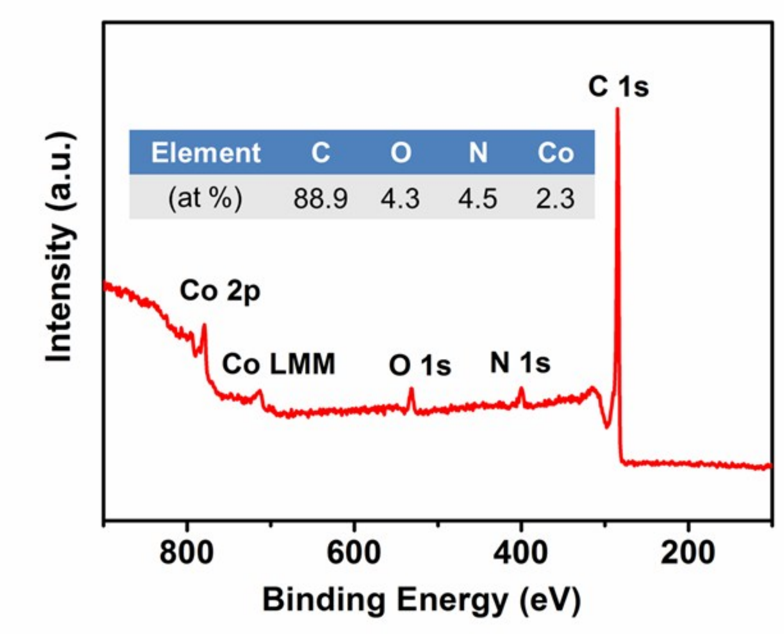

Element	C	O	N	Co
(at %)	88.9	4.3	4.5	2.3

Figure S7. XPS survey spectrum and the corresponding element contents for the Co-NC/CF.

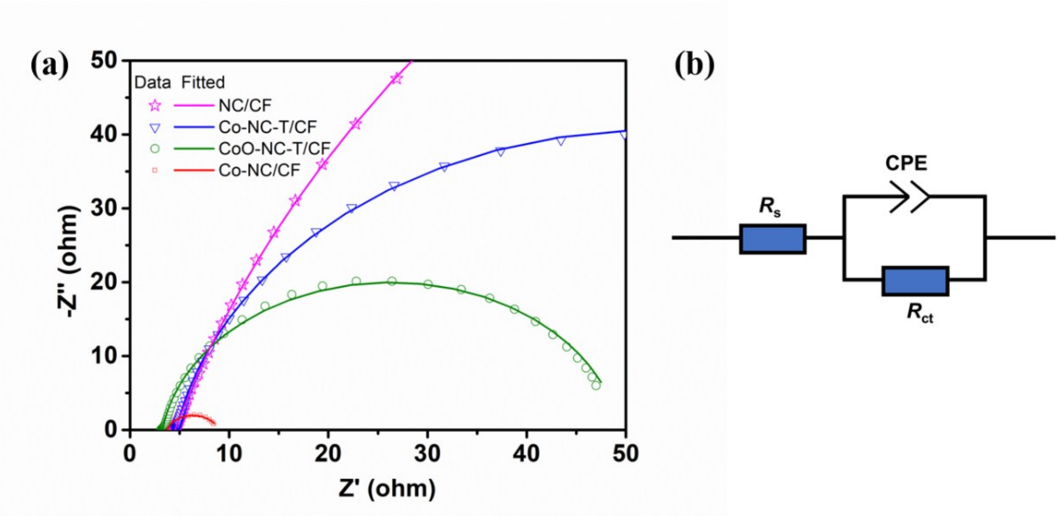

(c)

	Co-NC/CF	CoO-NC-T/CF	Co-NC-T/CF	NC/CF
R_s (ohm)	3.7	3.3	4.6	4.5
R_{ct} (ohm)	5.2	46.1	97.2	310.3

Figure S8. (a) EIS plots of NC/CF, Co-NC-T/CF, CoO-NC-T/CF, and Co-NC/CF recorded at a potential of 1.55 V vs. RHE. The symbols are experimental data and lines are fitted results by equivalent electrical circuit shown in (b); (b) equivalent electrical circuit used to fit the EIS data, consisting of a series resistance (R_s), a constant phase element (CPE), and R_{ct} related to OER process; (c) the fitted R_s and R_{ct} values from the EIS plots for NC/CF, Co-NC-T/CF, CoO-NC-T/CF, and Co-NC/CF.

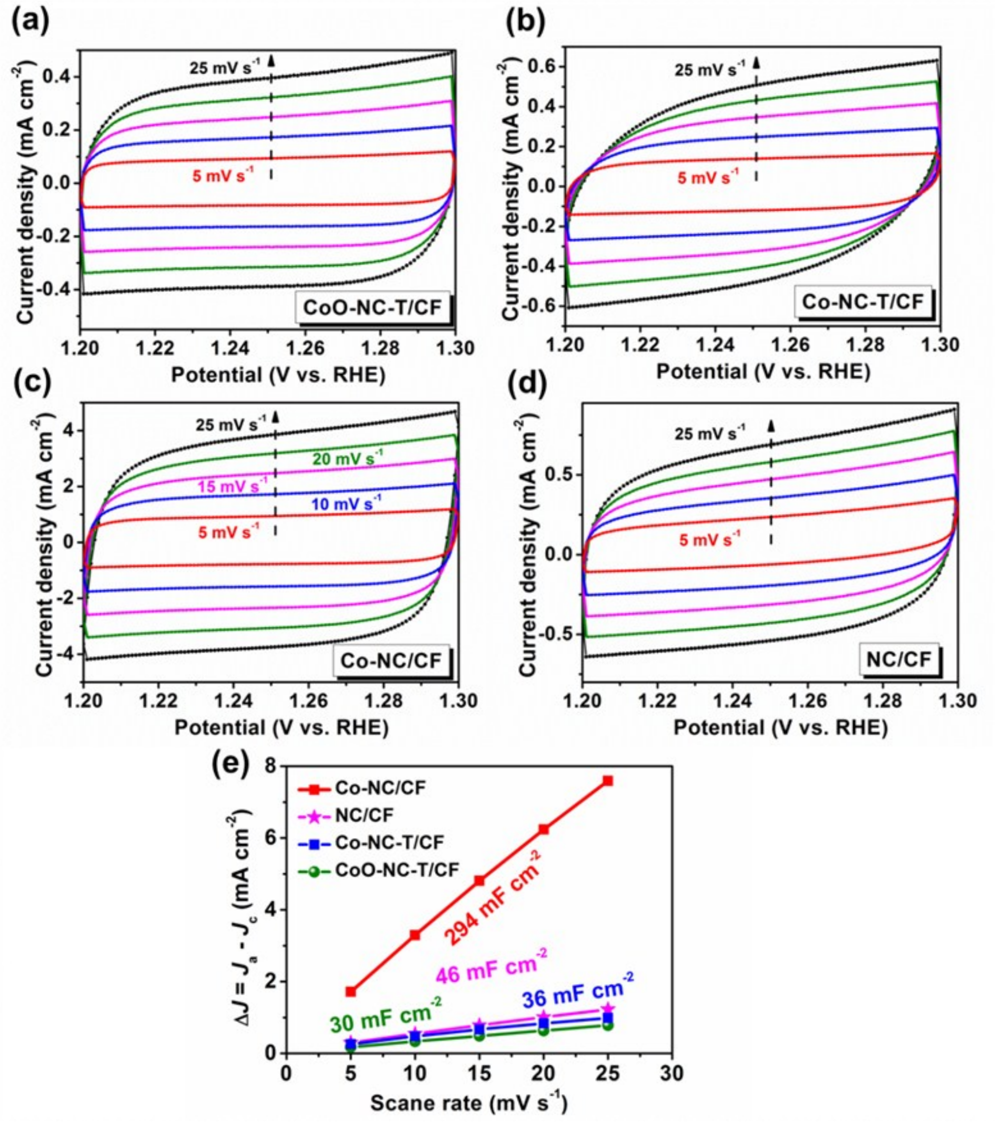

Figure S9. Electrochemical double-layer capacitance measurements: cyclic voltammetry curves from 1.20 to 1.30 V vs. RHE at scan rates ranging from 5, 10, 15, 20, to 25 mV s^{-1} for (a) CoO-NC-T/CF, (b) Co-NC-T/CF, (c) Co-NC/CF, and (d) NC/CF; (e) charging current density differences ($\Delta J = J_a - J_c$ at a potential of 1.25 V vs. RHE) plotted against scan rates for the as-made samples, of which the linear slope is equivalent to twice of the C_{dl}.

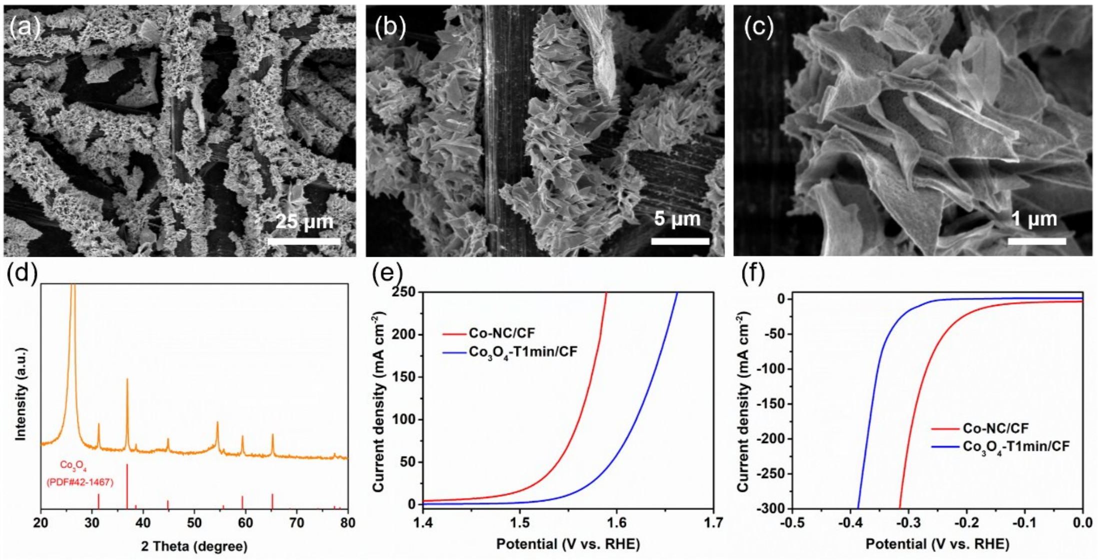

Figure S10. (a-c) SEM images and (d) XRD pattern of Co_3O_4-T1min/CF; (e) OER and (f) HER polarization curves for the Co-NC/CF and Co_3O_4-T1min/CF.

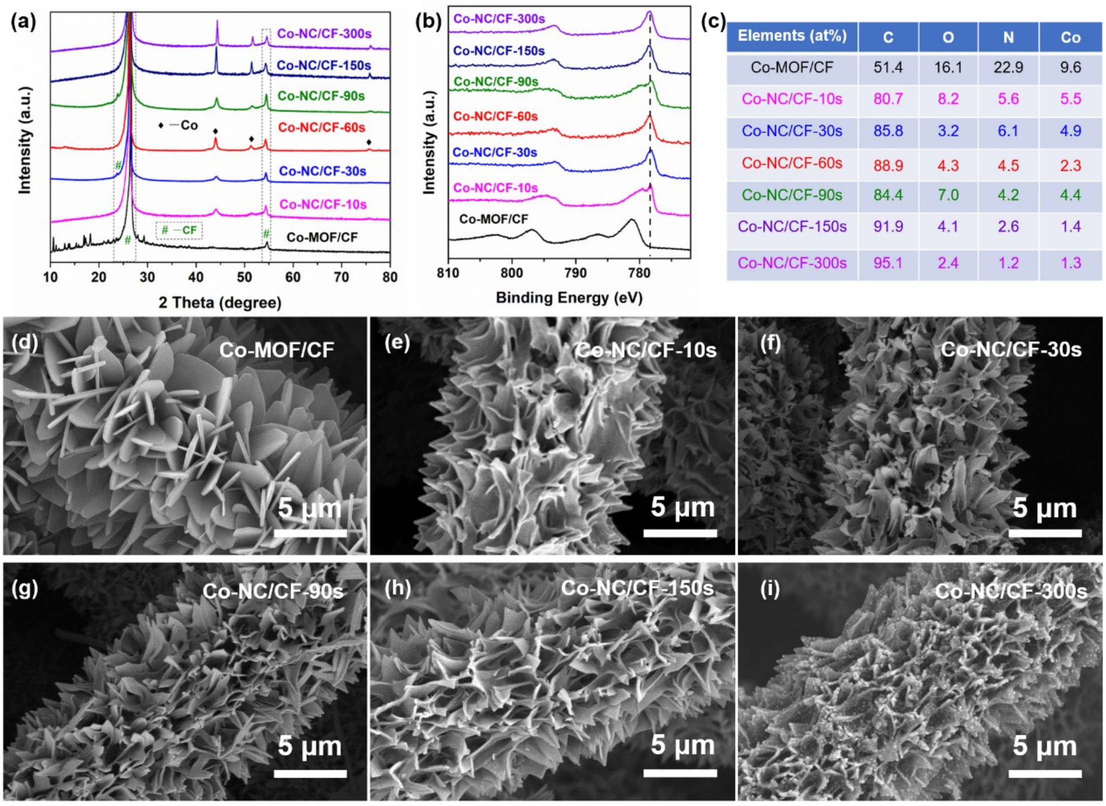

Elements (at%)	C	O	N	Co
Co-MOF/CF	51.4	16.1	22.9	9.6
Co-NC/CF-10s	80.7	8.2	5.6	5.5
Co-NC/CF-30s	85.8	3.2	6.1	4.9
Co-NC/CF-60s	88.9	4.3	4.5	2.3
Co-NC/CF-90s	84.4	7.0	4.2	4.4
Co-NC/CF-150s	91.9	4.1	2.6	1.4
Co-NC/CF-300s	95.1	2.4	1.2	1.3

Figure S11. (a) XRD patterns, (b) high resolution Co 2p XPS spectra, and (c) element contents derived from XPS results of Co-MOF/CF, Co-NC/CF-10s, Co-NC/CF-30s, Co-NC/CF-60s, Co-NC/CF-90s, Co-NC/CF-150s and Co-NC/CF-300s; SEM images of (d) Co-MOF/CF, (e) Co-NC/CF-10s, (f) Co-NC/CF-30s, (g) Co-NC/CF-90s, (h) Co-NC/CF-150s, and (i) Co-NC/CF-300s.

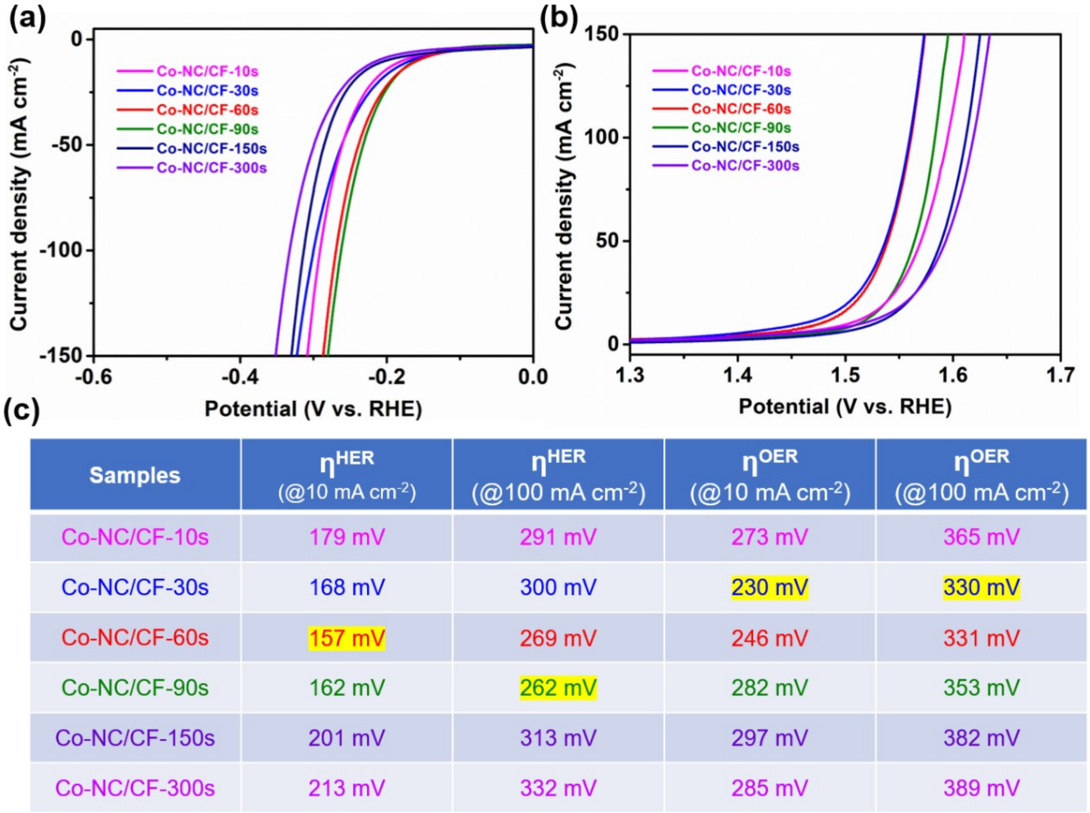

Samples	η^{HER} (@10 mA cm^{-2})	η^{HER} (@100 mA cm^{-2})	η^{OER} (@10 mA cm^{-2})	η^{OER} (@100 mA cm^{-2})
Co-NC/CF-10s	179 mV	291 mV	273 mV	365 mV
Co-NC/CF-30s	168 mV	300 mV	230 mV	330 mV
Co-NC/CF-60s	157 mV	269 mV	246 mV	331 mV
Co-NC/CF-90s	162 mV	262 mV	282 mV	353 mV
Co-NC/CF-150s	201 mV	313 mV	297 mV	382 mV
Co-NC/CF-300s	213 mV	332 mV	285 mV	389 mV

Figure S12. (a) HER, (b) OER polarization curves and (c) overpotentials at current densities of 10 and100 mA cm^{-2} for Co-NC/CF-10s, Co-NC/CF-30s, Co-NC/CF-60s, Co-NC/CF-90s, Co-NC/CF-150s, and Co-NC/CF-300s. In (c), the lowest overpotentials of samples were marked in luminous yellow color.

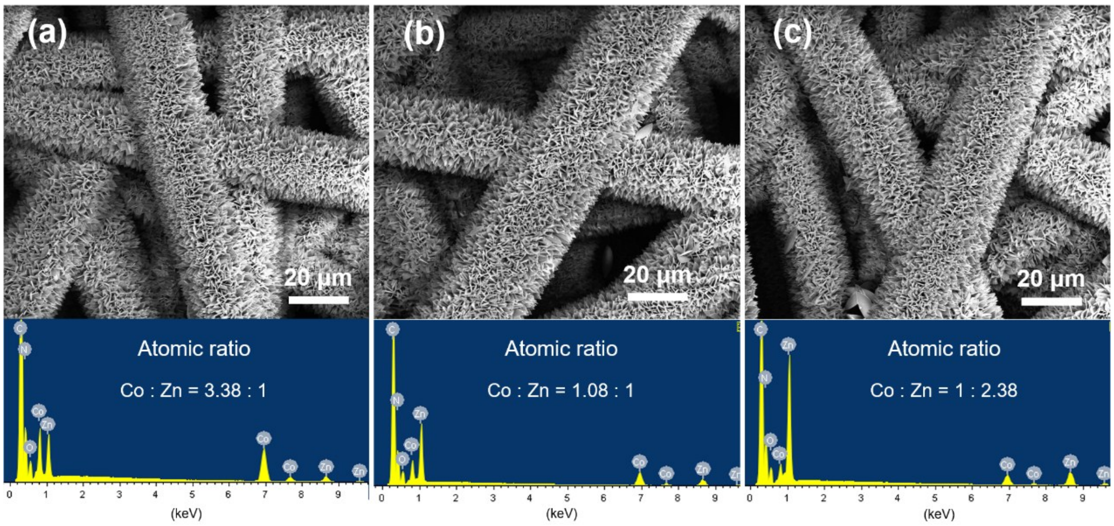

Figure S13. SEM images and the corresponding EDX element spectra of (a) Co_3Zn_1-MOF/CF, (b) Co_1Zn_1-MOF/CF, and (c) Co_1Zn_3-MOF/CF.

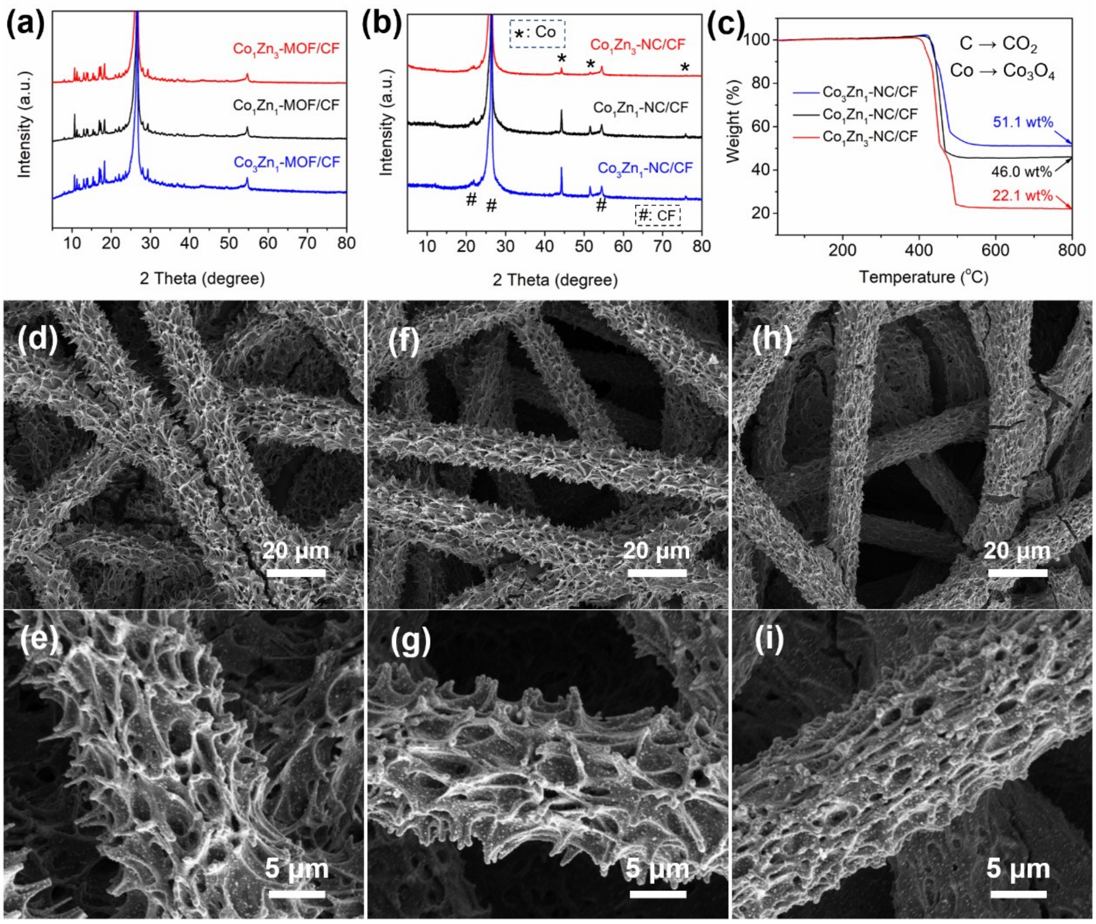

Figure S14. (a) XRD patterns of Co_3Zn_1-MOF/CF, Co_1Zn_1-MOF/CF, and Co_1Zn_3-MOF/CF; (b) XRD patterns of Co_3Zn_1-NC/CF, Co_1Zn_1-NC/CF, and Co_1Zn_3-NC/CF and (c) their TGA curves with a heating rate of 10 ^{o}C min^{-1} under air atmosphere; SEM images of (d, e) Co_3Zn_1-NC/CF, (f, g) Co_1Zn_1-NC/CF, and (h, i) Co_1Zn_3-NC/CF. In (c), the Co content of samples is calculated from the following equation: m (Co) = 3×M(Co)/M(Co_3O_4) × residual mass fraction. M(Co) and M(Co_3O_4) represented the molar mass of Co and Co_3O_4, respectively.

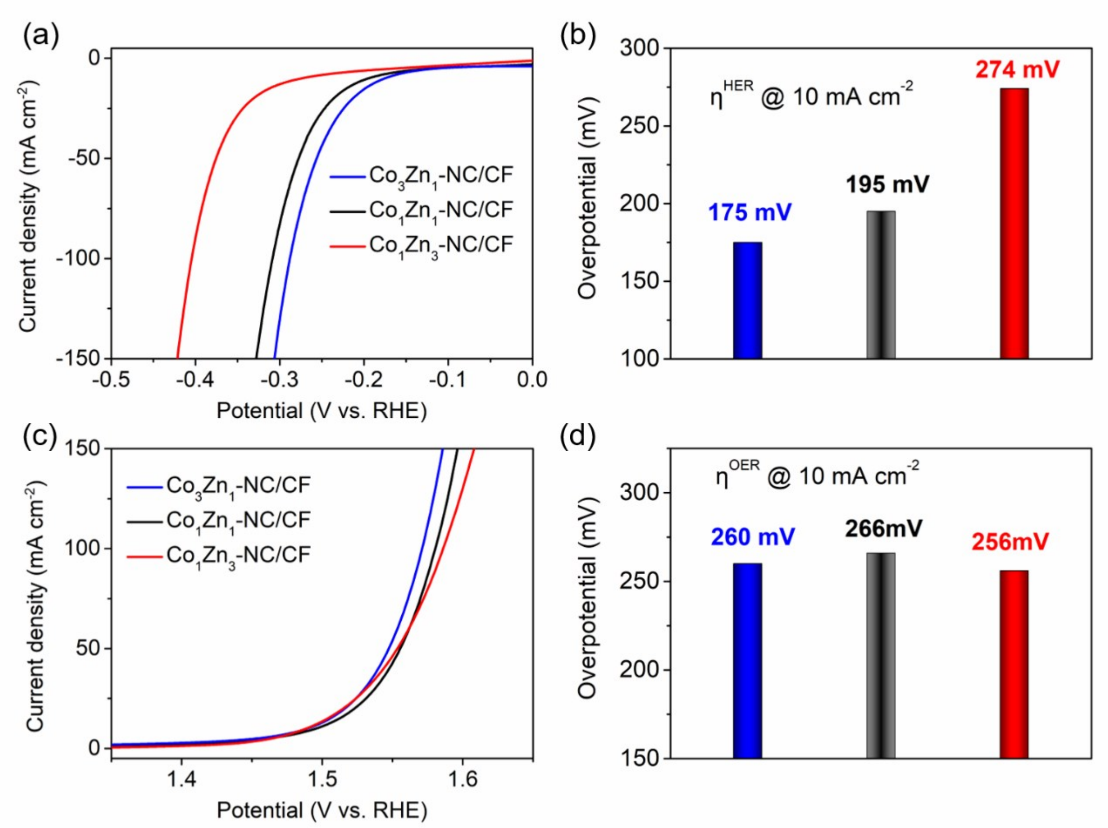

Figure S15. (a) HER and (c) OER polarization curves of Co_3Zn_1-NC/CF, Co_1Zn_1-NC/CF, and Co_1Zn_3-NC/CF; overpotentials at a current density of 10 mA cm^{-2} for (b) HER and (d) OER. In (b, d), the blue column represented Co_3Zn_1-NC/CF, the black column represented Co_1Zn_1-NC/CF, and the red column represented Co_1Zn_3-NC/CF.

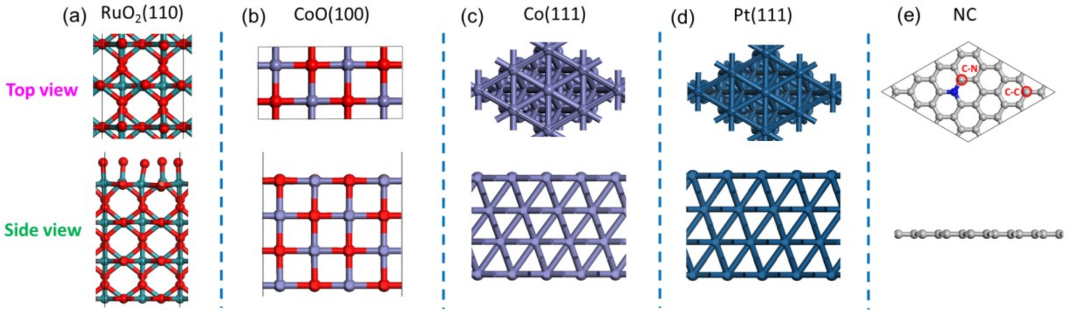

Figure S16. Model structures of (a) RuO_2, (b) CoO, (c) Co, (d), Pt, (e) NC.

The selected RuO_2 (110) and Pt (111) surfaces used for calculations are widely accepted for active sites for OER and HER, respectively.[10, 11] The CoO (100) surface is active for both OER and HER.[12, 13] The Co(111) surface and NC are calculated for comparison with NC grafted on Co(111) (Co-NC/CF).

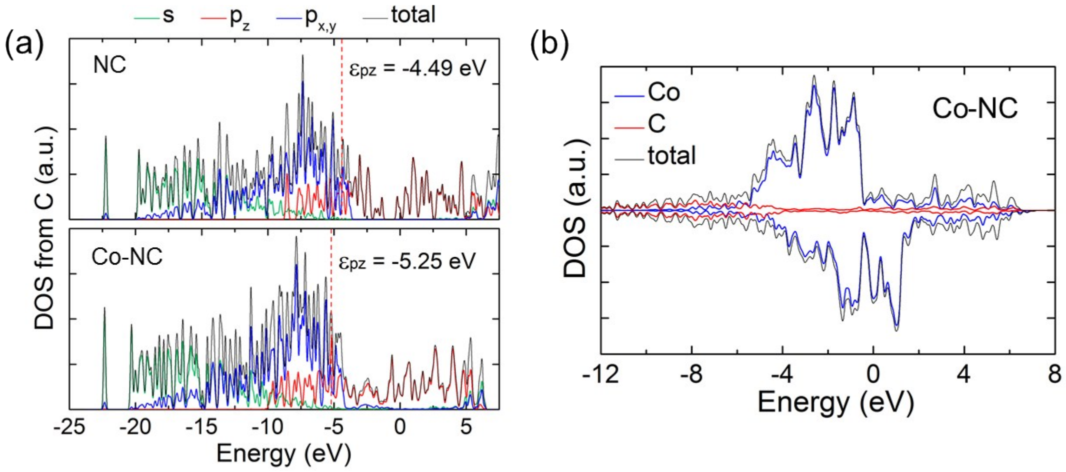

Figure S17. (a) Density of states (DOS) of C atoms in NC and Co-NC projected at different atomic orbitals. The red dashed lines and the number next to them indicates the p_z band center relative to the Fermi level. (b) DOS of Co-NC. The blue and red lines show the local DOS from Co and C atoms, respectively. The Fermi level is shifted to zero.

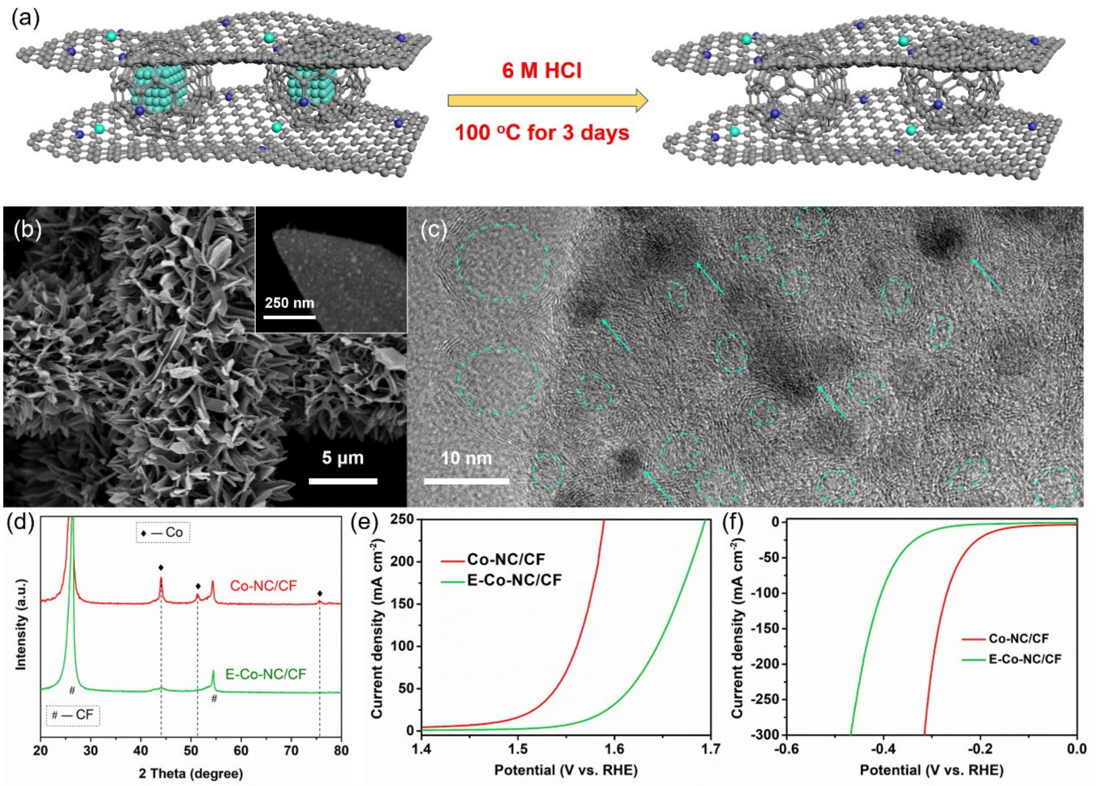

Figure S18. (a) Schematic illustration for etching of Co-NC/CF to E-Co-NC/CF; (b) SEM images and (c) HR-TEM image of E-Co-NC/CF; (d) XRD patterns, (e) HER and (f) OER polarization curves of Co-NC/CF and E-Co-NC/CF.

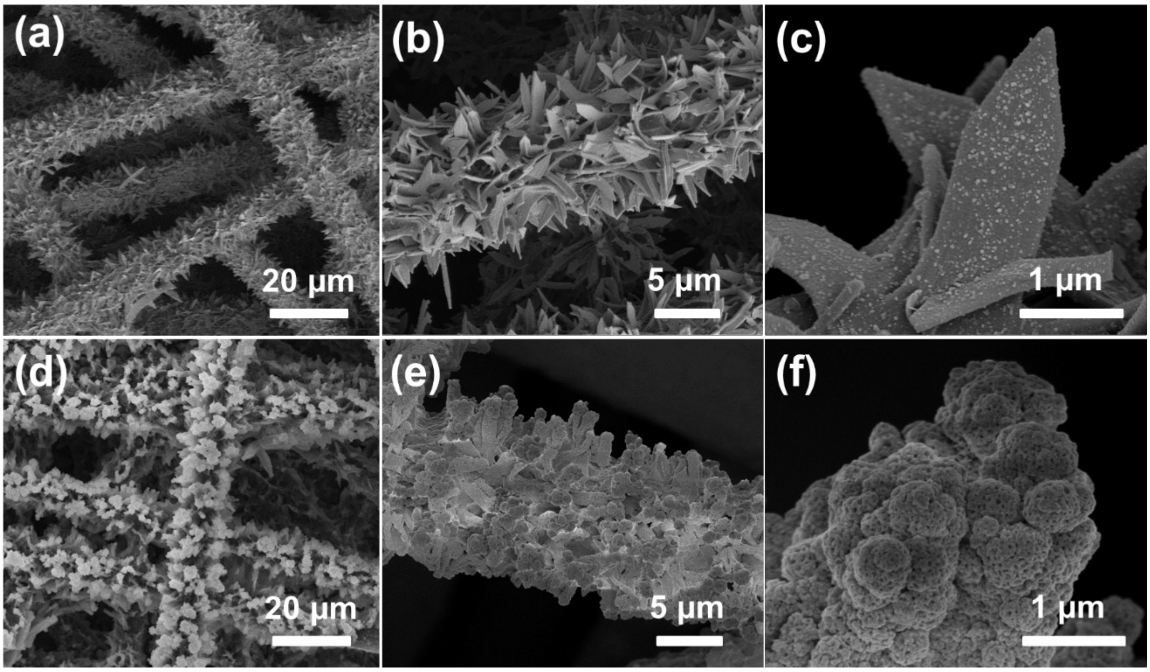

Figure S19. SEM images of (a-c) post-HER and (d-f) post-OER Co-NC/CF samples.

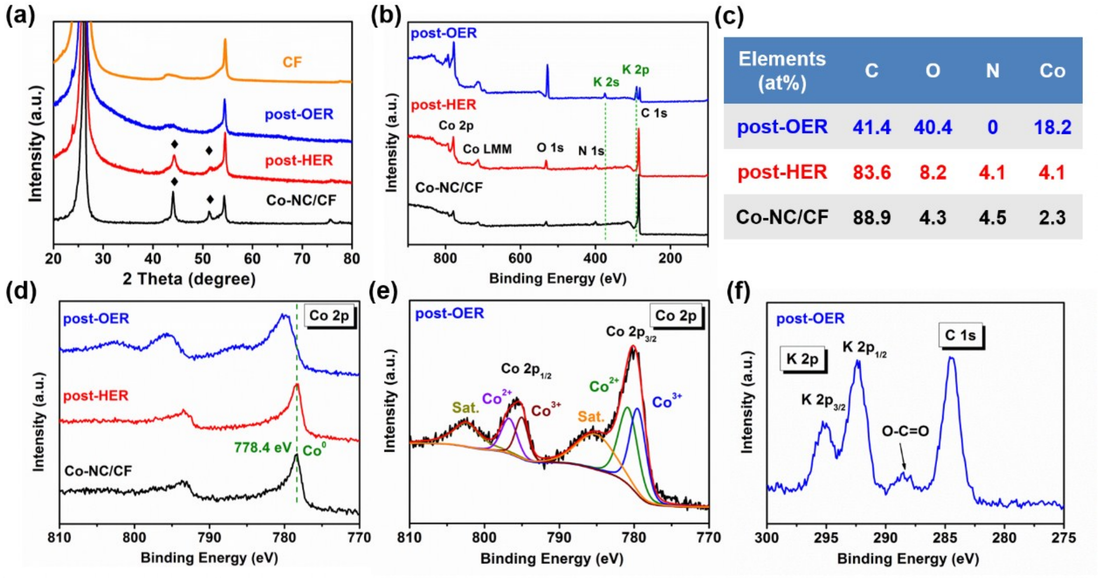

Elements (at%)	C	O	N	Co
post-OER	41.4	40.4	0	18.2
post-HER	83.6	8.2	4.1	4.1
Co-NC/CF	88.9	4.3	4.5	2.3

Figure S20. (a) XRD patterns of CF, post-OER, post-HER and Co-NC/CF; (b) XPS survey spectra, (c) element contents derived from XPS results, (d) high resolution Co 2p XPS spectra of Co-NC/CF, post-OER and post-HER Co-NC/CF samples; high resolution XPS spectra of (e) Co 2p, (f) K 2p and C 1s for post-OER Co-NC/CF sample.

Notes: The presence of element K is due to the fact that the partial KOH electrolyte penetrates into the porous post-OER Co-NC/CF sample and it is difficult to be completely washed out. Elements content calculated results of post-OER Co-NC/CF have excluded the content of K.

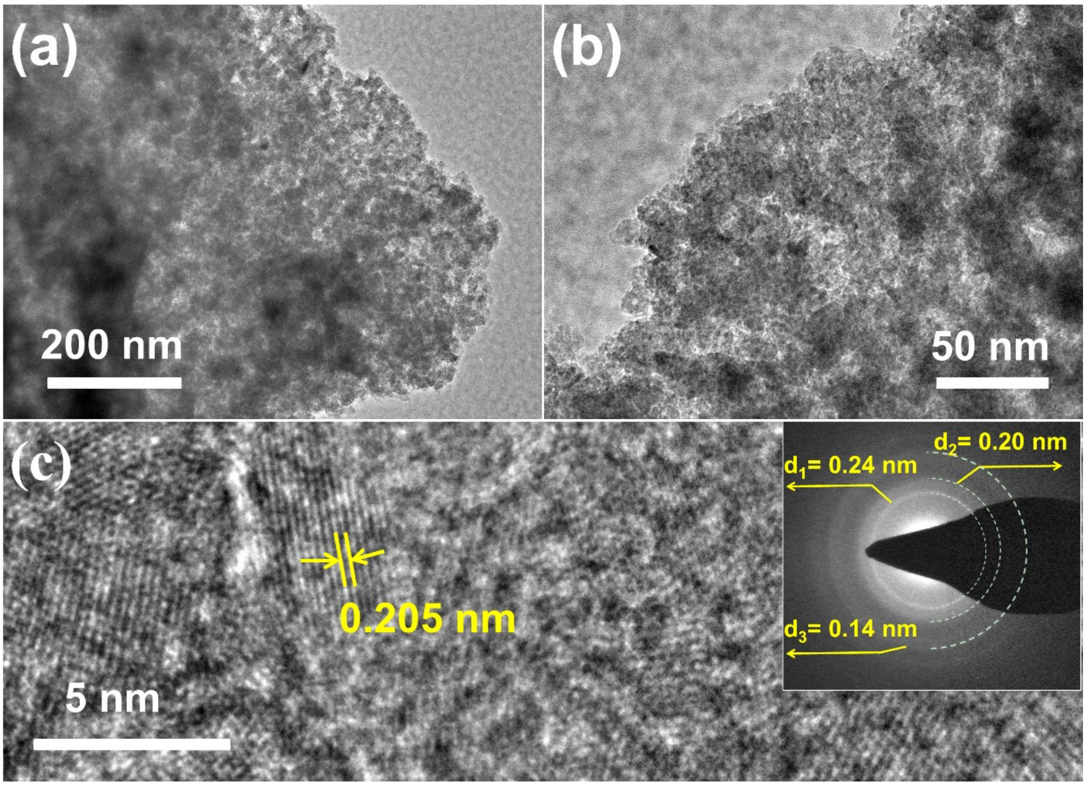

Figure S21. (a-c) TEM and HR-TEM images of post-OER Co-NC/CF sample. The inset corresponding SAED pattern indicated a typical low degree of crystallinity and polycrystalline characteristics of CoO_x grains.

The lattice spacing (d_1, d_2, d_3) calculated from the SAED pattern may correspond to (111) plane of CoO, (400) and (440) plane of Co_3O_4, respectively. This indicated that the Co-NC/CF catalyst has been oxidized during OER process.

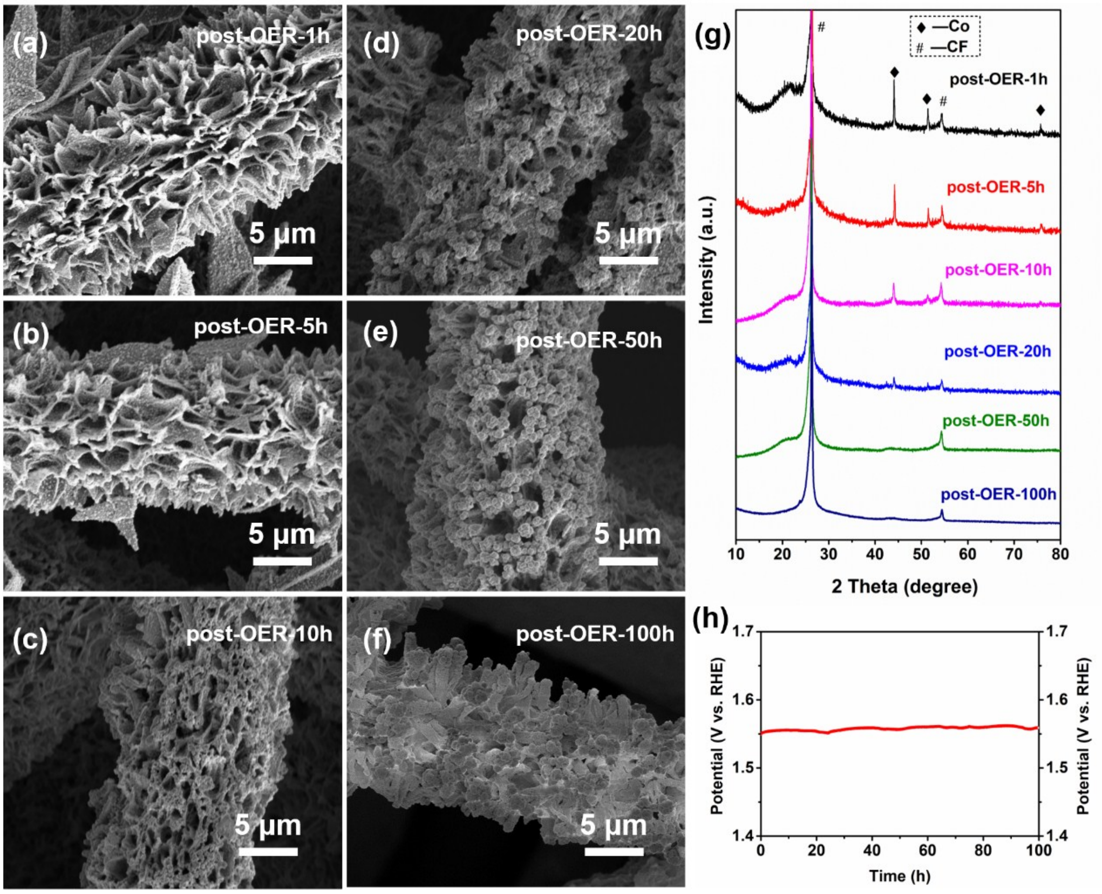

Figure S22. (a-f) SEM images and (g) XRD patterns of post-OER-1h, -5h, -10h, -20h, -50h, and -100h; (h) OER chronopotentiometry test of Co-NC/CF evaluated at 20 mA cm^{-2} without *iR* compensation.

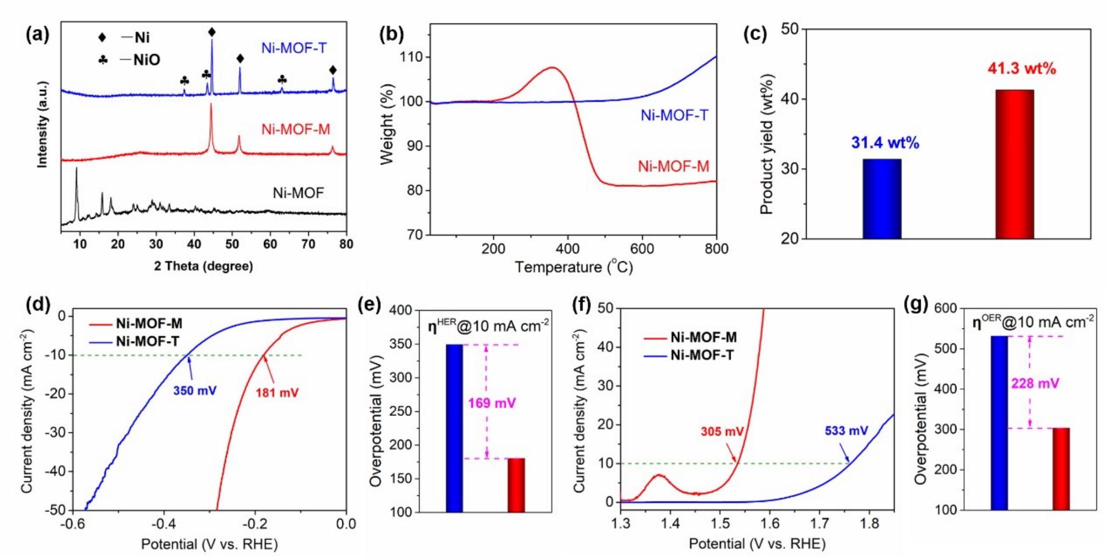

Figure S23. (a) XRD patterns of Ni-MOF, Ni-MOF-M, and Ni-MOF-T; (b) TGA curves of Ni-MOF-M and Ni-MOF-T with a heating rate of 10 ^{o}C min^{-1} under air atmosphere; (c) comparison of product yield for Ni-MOF-M and Ni-MOF-T derived from Ni-MOF; (d) HER and (f) OER polarization curves of Ni-MOF-M and Ni-MOF-T; overpotentials at a current density of 10 mA cm^{-2} for (e) HER and (g) OER. In (c, e, g), the blue column represented Ni-MOF-T, and the red column represented Ni-MOF-M.

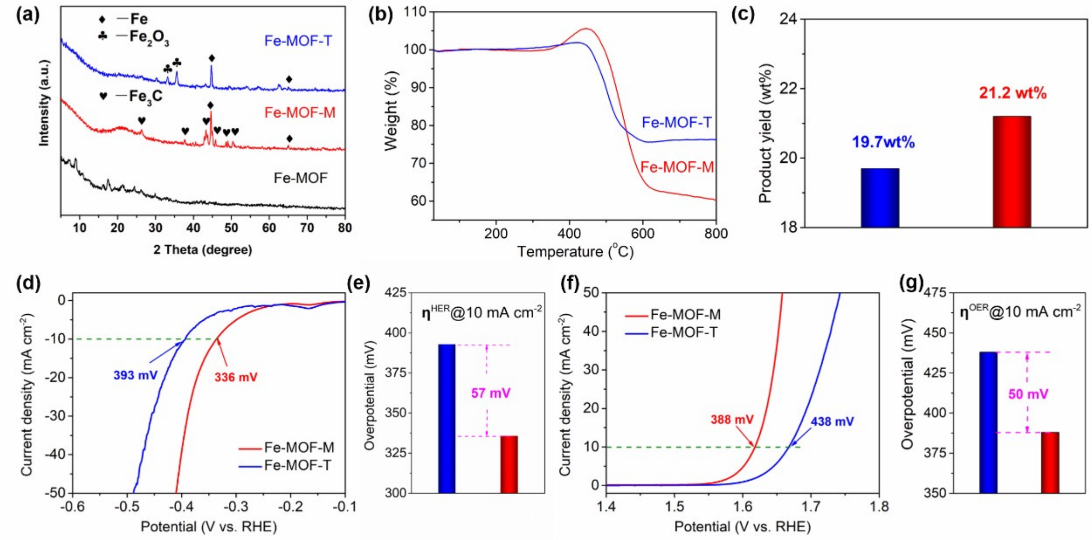

Figure S24. (a) XRD patterns of Fe-MOF, Fe-MOF-M, and Fe-MOF-T; (b) TGA curves of Fe-MOF-M and Fe-MOF-T with a heating rate of 10 ^{o}C min^{-1} under air atmosphere; (c) comparison of product yield for Fe-MOF-M and Fe-MOF-T derived from Fe-MOF; (d) HER and (f) OER polarization curves of Fe-MOF-M and Fe-MOF-T; overpotentials at a current density of 10 mA cm^{-2} for (e) HER and (g) OER. In (c, e, g), the blue column represented Fe-MOF-T, and the red column represented Fe-MOF-M.

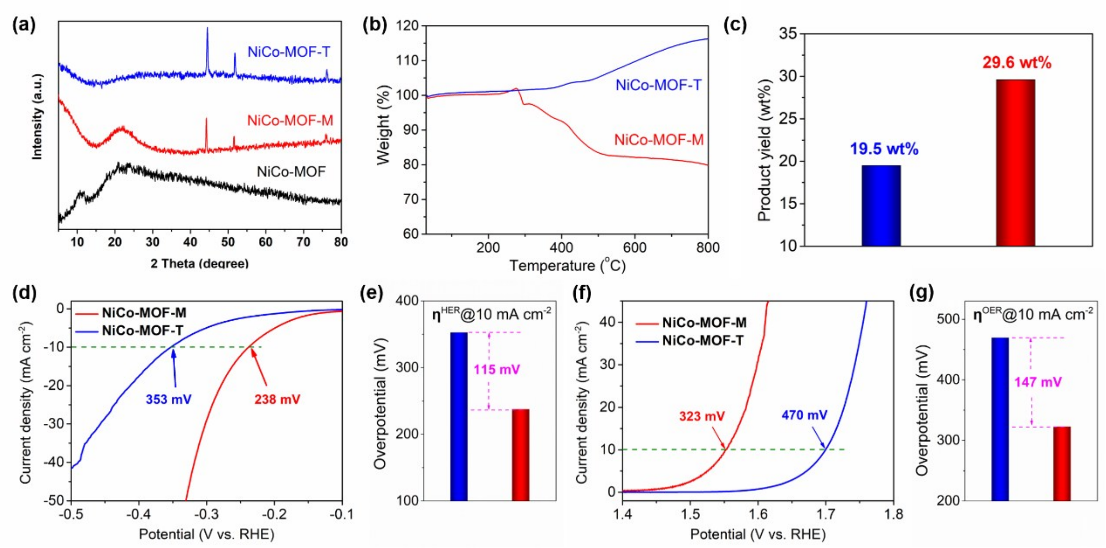

Figure S25. (a) XRD patterns of NiCo-MOF, NiCo-MOF-M, and NiCo-MOF-T; (b) TGA curves of NiCo-MOF-M and NiCo-MOF-T with a heating rate of 10 ^{o}C min^{-1} under air atmosphere; (c) comparison of product yield for NiCo-MOF-M and NiCo-MOF-T derived from NiCo-MOF; (d) HER and (f) OER polarization curves of NiCo-MOF-M and NiCo-MOF-T; overpotentials at a current density of 10 mA cm^{-2} for (e) HER and (g) OER. In (c, e, g), the blue column represented NiCo-MOF-T, and the red column represented NiCo-MOF-M.

Table S1. The OER and HER performance and preparation process comparison over MOF-derived catalysts.

Catalysts	OER (overpotential, mV@ 10 mA cm^{-2})	HER (overpotential, mV@ 10 mA cm^{-2})	Electrolyte	Mass loading (mg cm^{-2})	Pyrolysis time *(heating rate)*	Ref.
Co-NC/CF	**246**	**157**	**1 M KOH**	**1.1**	**1 min**	**This work**
Ni@CoO@CoNC	309	190	1 M KOH	4.0	350 °C for **2 h** followed by 500 °C for **2 h** *(2 °C min^{-1})*	***Chem.*** **2017,** 2, 791
Co@N-C	350	N.A.	0.1 M KOH	0.2	900 °C for **1 h** *(5 °C min^{-1})*	***Adv. Mater.*** **2018,** 30, 1705431
NF@NC-CoFe$_2$O$_4$/C	240	N.A.	1 M KOH	1.03	400 °C for **2 h** followed by 600 °C for **4 h** *(2 °C min^{-1})*	***Adv. Mater.*** **2017**, 29, 1604437
NC@Co-NGC DSNC	410	N.A.	0.1 M KOH	0.4	800 °C for **5 h** *(2 °C min^{-1})*	***Adv. Mater.*** **2017,** 29, 1700874

Catalysts	OER (overpotential, mV@ 10 mA cm^{-2})	HER (overpotential, mV@ 10 mA cm^{-2})	Electrolyte	Mass loading **(mg cm^{-2})**	Pyrolysis time *(heating rate)*	Ref.
MSZIF-900	337	233	1 M KOH (OER) 0.5 M H_2SO_4 (HER)	0.286	900 °C for **1 h** *(5 ^{o}C min^{-1})*	***Angew. Chem. Int. Ed.*** 2017, 56,13781
NiFe@NC	360	N.A.	1 M KOH	0.288	900 °C for **2 h** *(5 ^{o}C min^{-1})*	***Nano Energy*** **2017,** 39, 245
NC@GC	340	N.A.	1 M KOH	0.25	800 °C for **3 h** *(5 ^{o}C min^{-1})*	***Nano Energy*** **2016,** 30, 368
NCNTFs derived from ZIF-67	350	N.A.	1 M KOH	0.2	350 °C for **1.5 h** followed by 700 °C for **3.5 h** *(2 ^{o}C min^{-1})*	***Nat. Energy*** **2016,** 1, 15006

Notes: The heating rates used in most of the literature are 2-5 ^{o}C min^{-1}, so the total pyrolysis time is actually much longer, implying a longer preparation cycle and more energy consumption.

Table S2. Binding energies and adsorption free energies for H^* (ΔE_{H*} and ΔG_{H*}), binding energies of oxygenated intermediates (ΔE_{OH*}, ΔE_{O*} and ΔE_{OOH*}), OER overpotentials (η^{OER}), and rate-limiting step (RLS) involved in OER and HER processes for different model systems. The red numbers highlight the systems with relatively high activities for OER or HER.

Material	**ΔE_{H*} (eV)**	**ΔG_{H*} (eV)**	**ΔE_{OH*} (eV)**	**ΔE_{O*} (eV)**	**ΔE_{OOH*} (eV)**	**η^{OER} (V)**	**RLS**
RuO_2(110)	--	--	0.31	1.91	3.15	0.40	OOH*
Pt(111)	-0.33	-0.09	--	--	--	--	--
CoO(100)	0.94	1.18	0.90	2.74	4.07	0.50	OOH*
Co(111)	-0.72	-0.48	-2.46	1.22	2.04	2.07	O*
NC(C-C)	0.73	1.10	1.47	3.15	4.62	0.63	OH*
NC(C-N)	0.30	0.67	1.00	2.91	4.27	0.52	OOH*
Co-NC(C-C)	0.05	0.42	0.80	2.66	4.00	0.50	OOH*
Co-NC(C_2-N)	-0.05	0.32	0.72	2.60	3.89	0.44	OOH*
Co-NC(C_1-N)	-0.24	0.13	0.44	1.30	3.66	1.52	OOH*

References

1. H. Huang, C. Yu, C. Zhao, X. Han, J. Yang, Z. Liu, S. Li, M. Zhang and J. Qiu, *Nano Energy*, 2017, **34**, 472-480.
2. H. Sun, Y. Lian, C. Yang, L. Xiong, P. Qi, Q. Mu, X. Zhao, J. Guo, Z. Deng and Y. Peng, *Energy Environ. Sci.*, 2018, **11**, 2363-2371.
3. B. Y. Guan, L. Yu and X. W. Lou, *Energy Environ. Sci.*, 2016, **9**, 3092-3096.
4. L.-L. Wu, Z. Wang, Y. Long, J. Li, Y. Liu, Q.-S. Wang, X. Wang, S.-Y. Song, X. Liu and H.-J. Zhang, *Small*, 2017, **13**, 1604270.
5. G. Kresse and J. Furthmüller, *Phys. Rev. B*, 1996, **54**, 11169-11186.
6. G. Kresse and D. Joubert, *Phys. Rev. B*, 1999, **59**, 1758-1775.
7. J. P. Perdew, K. Burke and M. Ernzerhof, *Phys. Rev. Lett.*, 1996, **77**, 3865-3868.
8. S. Grimme, J. Antony, S. Ehrlich and H. Krieg, *J. Chem. Phys.*, 2010, **132**, 154104.
9. F. Meng, Z. Fang, Z. Li, W. Xu, M. Wang, Y. Liu, J. Zhang, W. Wang, D. Zhao and X. Guo, *J. Mater. Chem. A*, 2013, **1**, 7235-7241.
10. R. R. Rao, M. J. Kolb, N. B. Halck, A. F. Pedersen, A. Mehta, H. You, K. A. Stoerzinger, Z. Feng, H. A. Hansen, H. Zhou, L. Giordano, J. Rossmeisl, T. Vegge, I. Chorkendorff, I. E. L. Stephens and Y. Shao-Horn, *Energy Environ. Sci.*, 2017, **10**, 2626-2637.
11. T. F. Jaramillo, K. P. Jørgensen, J. Bonde, J. H. Nielsen, S. Horch and I. Chorkendorff, *Science*, 2007, **317**, 100.
12. T. Ling, D.-Y. Yan, Y. Jiao, H. Wang, Y. Zheng, X. Zheng, J. Mao, X.-W. Du, Z. Hu, M. Jaroniec and S.-Z. Qiao, *Nat. Commun.*, 2016, **7**, 12876.
13. T. Ling, D.-Y. Yan, H. Wang, Y. Jiao, Z. Hu, Y. Zheng, L. Zheng, J. Mao, H. Liu, X.-W. Du, M. Jaroniec and S.-Z. Qiao, *Nat. Commun.*, 2017, **8**, 1509.